Koch-Müller, M., Rhede, D., Schulz, R., Wirth, R. (2009): Breakdown of hydrous ringwoodite to pyroxene and spinelloid at high P and T and oxidizing conditions. - Physics and Chemistry of Minerals, 36, 6, 329-341

DOI: 10.1007/s00269-008-0281-z

Breakdown of hydrous ringwoodite to pyroxene and spinelloid at high P and T and oxidizing conditions

M. Koch-Müller, D. Rhede, R. Schulz, R. Wirth

Deutsches GeoForschungsZentrum Potsdam, Department 4, Telegrafenberg, 14473 Potsdam, Germany

For **Physics and Chemistry of Minerals**

Key words: Fe_2SiO_4 spinel, Spinelloid III and V, Wadsleyite, HP experiments, Multi-anvil apparatus, Raman- and IR spectroscopy

Corresponding author:
Monika Koch-Müller
Deutsches GeoForschungsZentrum Potsdam
Department 4, Chemie der Erde
Telegrafenberg
14473 Potsdam
Germany

Phone + 49 (331) 288-1492
Fax + 49 (331) 288-1402

mkoch@gfz-potsdam.de

Abstract

To get deeper insight into the phase relations in the end-member system Fe_2SiO_4 and in the system $(Fe, Mg)_2SiO_4$ experiments were performed in a multi-anvil apparatus at 7 and 13 GPa and 1,000 –1,200°C as a function of oxygen fugacity. The oxygen fugacity was varied using the solid oxygen buffer systems Fe/FeO, quartz-fayalite-magnetite, MtW and Ni/NiO. The run products were characterized by electron microprobe, Raman- and FTIR-spectroscopy, X-ray powder diffraction and transmission electron microscopy. At fO_2 corresponding to Ni/NiO Fe-ringwoodite transforms to ferrosilite and spinelloid according to the reaction: $9\ Fe_2SiO_4 + O_2 = 6\ FeSiO_3 + 5\ Fe_{2.40}Si_{0.60}O_4$. Refinement of site occupancies in combination with stochiometric Fe^{3+} calculations show that 32% of the total Fe is incorporated as Fe^{3+} according to $(Fe^{2+}_{1.60}Fe^{3+}_{0.40})^{VI}(Si_{0.60}Fe^{3+}_{0.40})^{IV}O_4$. From the Rietveld refinement we identified spl as spinelloid III (isostructural with wadsleyite) and/or spinelloid V. As we used water in excess in the experiments the run products were also analyzed for structural water incorporation. Adding Mg to the system increases the stability field of ringwoodite to higher oxygen fugacity and the spinel structure seems to accept higher Fe^{3+} but also water concentrations that may be linked. At oxygen fugacity corresponding to MtW conditions similar phase relations in respect to the breakdown reaction in the Fe-end-member system were observed but with a strong fractionation of Fe into spl and Mg into coexisting cpx. Thus, through this strong fractionation it is possible to stabilize very Fe-rich wadsleyite with considerable Fe^{3+} concentrations even at an intermediate Fe-Mg bulk composition: assuming constant K_D independent on composition and a bulk composition of $x_{Fe} = 0.44$ this fractionation would stabilize spl with $x_{Fe} = 0.72$. Thus, spl could be a potential Fe^{3+} bearing phase at P-T conditions of the transition zone but because of the oxidizing conditions and the Fe-rich bulk composition needed one would expect it more in subduction zone environments than in the transition zone in senso stricto.

Introduction

The stability relations in the systems M_2SiO_4 (M = Mg, Fe, Ni, Co) were the subjects of numerous studies (e.g., Ringwood and Major 1966; Akimoto and Ida 1966; Suito 1972; Yagi et al. 1974; Ohtani 1979; Morishima et al. 1994; Fei and Bertka 1999) because of their significance for the mantle transition zone. In the Mg_2SiO_4 system, three polymorphs exist: at ambient conditions olivine, at pressure > 13 GPa (1,000°C) wadsleyite in a modified spinel structure (spinelloid, spl) and at P > 18 GPa (1,000°C) ringwoodite in the true spinel (sp) structure (e.g., Morishima et al. 1994). This is quite different to the Fe_2SiO_4 system where no intervening wadsleyite phase was observed but fayalite directly transforms to Fe-ringwoodite at 5.3 GPa (1,000°C) (e.g., Akimoto et al. 1965). On the other hand, Woodland and Angel (1998) performed experiments at 5.6 GPa and 1,100°C using a mixture of fayalite and magnetite as starting material and were able to synthesize an spl which is isostructural with wadsleyite but which incorporates a significant amount of Fe^{3+}. Five different spinelloid modifications are known, e.g., from the system $NiAl_2O_4$-Ni_2SiO_4 (Ma 1974) and are designated as spinelloid I-V. They all are based on a cubic close-packed oxygen sublattice with ideal A_2BO_4. But they differ in the stacking order of the structural unit, which consists of a tetrahedral site and two octahedral sites. Experiments e.g., Woodland and Angel (2000) revealed that in the system Fe_2SiO_4-Fe_3O_4 three spinelloid polytypes isostructural to spinelloid II, III and V exist. In all these spl structures Si^{IV} is partly replace by Fe^{3+} and for charge balancing the same amount of Fe^{2+} pfu in the M sites is replace by Fe^{3+}. Yamanaka et al. (1998, 2001) and van Aken and Woodland (2006), observed in spl V in addition to the above-mentioned substitution of Si^{4+} by Fe^{3+} a disorder of Si^{4+} over the tetrahedral and octahedral sites. According to Yamanaka and Okita (2001), Si^{4+} can occupy 7% of the octahedral site in spl V. However, the geologically most important spinelloid modification is spl III, which is isostructural with wadsleyite. The experiments by Woodland and Angel (1998) show that Fe-wadsleyite can only be stabilized if significant amounts of Fe^{3+} are

incorporated. Koch et al. (2004) added the component Mg_2SiO_4 to the system Fe_2SiO_4-Fe_3O_4 and observed between 4 and 9 GPa and 1,100°C three intermediate phases of the spinelloid polytypes, namely spl II, III and V. According to their observations, the maximum Mg content of spl III is limited to 15 mol% Mg_2SiO_4.

Although such Fe^{3+}-rich spl has never been found in nature it may be an important Fe^{3+}-bearing phase in pyrolite upper mantle at about the transition zone (Yamanaka et al. 2001; Koch et al. 2004). Therefore an understanding of its crystal chemistry and stability in general as well as knowledge of its physical properties, e.g., electrical conductivity and magnetic properties is important for understanding geophysical processes in the Earth's upper mantle. To get deeper insight into the phase relations in the end-member system Fe_2SiO_4 as well as in the system Mg_2SiO_4-Fe_2SiO_4 we performed experiments at 7 and 13 GPa, and 1,000 – 1,200°C as a function of the oxygen fugacity. We would like to answer the following questions: what happens if we expose γ-Fe_2SiO_4 to high P and T and oxidizing conditions? Does it break down to magnetite plus free SiO_2 as its polymorph α-Fe_2SiO_4 or via a reaction in which Fe^{3+}-spl is involved? What are the exact conditions of the breakdown and what are the compositions of the products? What happens in respect to its oxidation in a more Mg-rich system?

Experimental

Experiments were performed in a multi-anvil apparatus similar to that of Walker (1991) but with a special tool which allows a continuous 360° rotation of the high-pressure module during the run duration with 1-5° s^{-1} in order to avoid separation of the fluid from the solid parts of the run (see Schmidt and Ulmer 2004). However, most of the experiments in the present study were performed in the static mode – one experiment (MA-36) has been rotated with 4° s^{-1}. Depending on the desired pressure we used the 18/11 and 14/8 assemblies (octahedron edge length/truncated edge length), consisting of a MgO-based octahedral

pressure medium with a stepped graphite heater and pyrophyllite gaskets. Pressure assemblies were calibrated at room temperature against the phase transitions in Bi metal (Lloyd 1971; Piermarini and Block 1975). Calibrations at higher temperature are based on the following phase transitions $CaGeO_3$ garnet-perovskite (Susaki et al. 1985); SiO_2 coesite–stishovite (Akaogi et al. 1995); Mg_2SiO_4 $\alpha-\beta$ transition (Morishima et al. 1994). The temperature was measured using a W5%Re-W26%Re thermocouple. No correction of the emf as a function of pressure was applied.

As starting material, we used either oxide mixtures (FeO, MgO and SiO_2) or synthetic fayalite, or a mixture of fayalite and oxides (MgO, SiO_2). One run (MA-51) was a reversed run, where we used synthetic Fe-ringwoodite as starting material. The starting materials were placed in Pt capsules that were pretreated with Fe to avoid or at least reduce loss of iron during the experiment. To produce different oxygen fugacities experiments were performed by modifying the double capsule technique as described by Koch-Müller et al. (2003): we placed water and a solid oxygen buffer at the bottom of the capsule and separated it mechanically by a Pt disk from the starting material above. One run was performed by simply adding graphite plus water to the starting material. Another run was performed without water but with the NNO buffer. We are quite sure that even in this run the oxygen fugacity produced by the solid buffer governed also the conditions in the sample chamber as the separation of buffer from the starting material was only mechanically. We verified the presence of excess water at the end of each experiment by placing the recovered and opened Pt capsule in an oven at 170°C and checking the weight difference before and after heat treatment. X-ray diffraction on tiny amounts of the buffer material using a Rigaku R/AXIS-SPIDER X-ray diffractometer with rotating anode indicated that in all cases the buffer was not exhausted during the run.

Figure 1 shows solid-state reactions that produce oxygen as log fO_2 versus temperature diagrams at room pressure, 7 and 13 GPa calculated using the database and software of

Chatterjee et al. (1998). Thermodynamic data for Ni and NiO were not included in the database and were taken from Robie et al. (1979). The quartz-fayalite-magnetite (QFMt) buffer is not stable at high pressures and temperatures and may transform to ferrosilite-magnetite-Fe-ringwoodite (FsMtFRng) at 7 GPa or stishovite-magnetite-Fe-ringwoodite (SMtFRng) at 13 GPa.

For quantitative chemical analyses, the samples were embedded in epoxy resin, polished and analyzed with a JEOL Hyperprobe JXA-8500F electron microprobe (EMP) operating in wavelength-dispersive mode. The conditions were an accelerating voltage of 15 kV, a beam current of 10 nA and a focused beam spot. The peak counting times were 30 s for Mg and Si, 40 s for Fe and the half time for background on either side of the peak. Standards were natural and synthetic minerals (e.g., periclase, forsterite, fayalite, diopside) and matrix corrections were performed following the Armstrong-CITZAF method. In order to overcome the density difference between a normal olivine standard and its high-pressure modification, a well-characterized synthetic ringwoodite was used as standard for Si, Mg and Fe.

For X-ray diffraction the experimental products were ground in an agate mortar for several minutes, diluted with Elmer´s white glue and evenly spread on a circular foil. Final size of the grains was about 5 μm. To minimize preferential orientation the powder was stirred during drying. Finally, the foil was placed into the transmission sample holder and covered with a second empty foil. Powder XRD patterns were recorded in transmission using a fully automated STOE STADI P diffractometer (Cu $K_{\alpha 1}$ radiation), equipped with a primary monochromator and a 7°-wide position sensitive detector. The normal-focus Cu X-ray tube was operated at 40 kV and 40 mA, using a take-off angle of 6°. Intensities were recorded in the range of 2θ of 9 to 125° with a detector step size of 0.1° and a resolution of 0.02°. A 1-mm thick Al-foil was placed in front of the detector in order to reduce fluorescence radiation in the Fe-rich samples. Counting times were selected to yield a maximum intensity of 3,000 counts. Unit cell parameters and other structural parameters were refined using the *GSAS*

software package for Rietveld refinements (Larson and Von Dreele 1987). The peaks were defined as pseudo-Voight with variable Lorentzian character. The recorded peaks were highly symmetric due to the geometry of the STADI P diffractometer, therefore no parameters describing the asymmetry of the peaks had to be used. Background was fitted with a real space correlation function that is capable of modeling the diffuse background from the amorphous foil and glue used for the preparation. Starting values for the refinements were the fractional atomic coordinates and lattice constants for Fe-ringwoodite (Yamanaka 1986), spinelloid III (Woodland and Angel 1998) and spinelloid V (Ross et al. 1992). The isotropic displacement parameters were set to 0.025. Due to the high background and the presence of multiple phases (two different modifications), only the lattice constants and phase fractions were refined. For experiments with more then 70 wt% sp also the parameter *u* was refined.

For TEM investigations, site-specific foils were prepared by focused ion beam technique (FIB). The instrument used was a FEI FIB200 with Ga-ion source operating at 200 kV. TEM was performed using a FEI Tecnai^{TM}G^2 F20 X-Twin transmission electron microscope equipped with a Gatan imaging filter and an EDAX-X-ray spectrometer. EEL spectra were acquired with a dispersion of 0.1 eV per channel. The energy resolution of the filter was 0.9 eV at half width at full maximum of the zero loss peak. Spectra were acquired in diffraction mode with an acquisition time of 1 s.

The polished microprobe samples were also used to record Raman spectra with a multichannel Raman microprobe (LabRAM HR800 UV-VIS spectrometer, 1,800 grooves/mm) in a backscattering configuration using a CCD detector (1,024 elements), an argon laser and an Olympus optical microscope with a long working distance 100x objective. For sample excitation, we used the 488 nm line. The confocal hole of the LabRAM HR800 spectrometer was variably chosen (100 - 200 μm) according to requirements. To prevent melting of the samples under the laser beam we used in addition to low laser power (80 mW)

density filters D1 (incident power/10) and D2 (incident power/100). Spectra acquisition time varied from 5 x 20 to 10 x 80 sec.

Doubly polished wafers of the run products were prepared and spectra were collected in the NIR-MIR regions on a Bruker IFS 66v FTIR spectrometer using an attached Hyperion microscope. The spectra were recorded with a resolution of 2 cm^{-1} from 256 scans with KBr beamsplitter and InSb (NIR) and MCT (MIR) detectors. Due to the lack of specific absorption coefficients for sp and spl, the water content was quantified using the general calibration by Libowitzky and Rossman (1997). For ferrosilite (fs) we took the omphacite calibration by Koch-Müller et al. (2007), i.e., an absorption coefficient of 65,000 l mol^{-1} H_2O cm^{-2}. MIR spectra of the lattice modes were taken on thin films, which were obtained by crashing crystals in a diamond anvil cell without a gasket.

From symmetry analysis we expect for cubic ringwoodite with two formula units in the primitive cell 42 normal modes (3 x 14). Experiments show five distinct Raman modes which can be divided among the symmetry species A_{1g} + E_g+ $3T_{2g}$ (e.g., Chopelas et al. 1994; Yu and Wentzcovitch 2006) and four distinct infrared modes of symmetry $4T_{1u}$ (e.g., Akaogi et al. 1984). For orthorhombic spinelloid with four formula units in the primitive cell 84 normal modes (3 x 28) are expected. The 74 Raman and/or IR active optical modes can be divided among the following symmetry species: $11A_g$ (R) + $7B_{1g}$ (R) + $9B_{2g}$ (R) + $12B_{3g}$ (R) + $13B_{1u}$ (IR) + 12 B_{2u} (IR) + 10 B_{3u} (IR).

Results

Table 1 lists the starting materials, the experimental conditions and products of the runs as well as results of X-ray diffraction studies. In principle, one would expect from Fig. 1 that the reactions FsMtFRng or SMtFRng represent the breakdown of Fe-ringwoodite at high oxygen fugacity. However, our experiments show that at lower oxygen fugacity than produced by FsMtFRng and SMtFRng another reaction with spl instead of magnetite takes place. Fe-

ringwoodite is the stable phase at relatively low oxygen fugacities (around IW corresponding to fO_2 of $10^{-11.8}$ bar at 1,000°C and 7 GPa) while it breaks down to spinelloid plus ferrosilite (fs) at oxygen fugacities around NNO at 1,000 and 1,200°C (fO_2 $10^{-7.3}$ and $10^{-5.0}$) according to the reaction 9 $Fe_2SiO_4 + O_2 = 6\ FeSiO_3 + 5\ Fe_{2.40}Si_{0.60}O_4$. Table 2 compiles the compositions of the run products according to EMP analyses. In a first step, we calculated all Fe as Fe^{2+}. However, doing so, the sum of the EMP analyses of the spinelloid phase was around 98%, which could be explained by a high Fe^{3+} concentration. Therefore we took EEL spectra on spl III and fs of sample MA-27 in the region of the Fe-L_{23} edge (680 - 780 eV) and the O-K edge (500 - 600 eV). According to van Aken and Liebscher (2002) the energy-loss structures of the Fe-L_{23} edges provides chemical information about the iron oxidation state. For Fe^{2+} in almandine the L_3-edge displays a maximum at 707.8 eV and Fe^{3+} in andradite has a characteristic Fe-L_3 edge at 709.5 eV. In spinel solid solutions the Fe-L_3 spectra exhibit only one asymmetric peak due to strong charge-transfer interactions between Fe^{2+} and Fe^{3+}. Compared to the EEL spectrum of fs that of spl III is indeed characterized by a higher asymmetry and higher half width at half maximum of 3.0 eV versus 2.5 eV for fs indicating the presence of Fe^{3+} in the structure (Fig. 2a, b). Compared to the O-K edge spectrum of fs a clear prepeak of the O-K edge can be observed in the spl III spectrum (Fig. 2c, d). This prepeak is indicative of both OH (Wirth 1997) and for Fe^{3+} (van Aken et al. 1998). As the amount of water in cpx and spl III is relatively low and equal (see below) we take the prepeak as additional proof of Fe^{3+}. There is no indication for Fe^{3+} in fs coexisting with spl (Fig. 2). Therefore we recalculated the EMP analyses (for sp and spl) by increasing the Fe^{3+} content in expense of Fe^{2+} until the cation sums up to 3.0, thus assuming a stoichiometric composition, e.g. for spl $(Fe^{2+}_{1.60}Fe^{3+}_{0.40})^{VI}(Si_{0.60}Fe^{3+}_{0.40})^{IV}O_4$. Due to these recalculations the oxide sum of the EMP analyses for spl increases from around 98 to 100%. Table 2 shows that these calculations work perfectly as the resulting formula could always be written as $(Fe^{2+}_{2-x}Fe^{3+}_{x})(Fe^{3+}_{x}Si^{4+}_{1-x})$. According to van Aken and Woodland (2006) the Fe^{3+}

concentration calculated from the Si/Fe concentration ratios assuming a stoichiometric composition of the spinelloids gives reasonable results. Under NNO conditions at 7 GPa and in the temperature range 1,000 – 1,200°C spl seems to be a stable phase coexisting with fs. The Si contents vary from 0.61 to 0.74 Si pfu. From X-ray diffraction, it became obvious that in three of five runs which produced spinelloid the spinelloid V modification was found. But in run MA-27 and run MA-51 two spl modifications, spl III and V coexist. In the EMP analyses we could, however, not distinguish between the two modifications. Within one run the compositions of spl were quite homogenous (Table 2). As we added water to the system that was incorporated into the crystals (see below) the calculated Fe^{3+} content may be slightly overestimated due to possible vacancies to account for the water content. One experiment has been performed without adding water and we also observed the breakdown to spl plus fs, indicating that the presence of water has no effect on the reaction.

Experiments in the system $(Fe, Mg)_2SiO_4$ were performed at 13 GPa as adding Mg to the Fe-end member system shifts the phase boundary between olivine and ringwoodite to higher pressures. At 13 GPa and temperature of 1,000 to 1,200°C we are with compositions ranging from x_{Fe} = 0.78 to 0.39 in all cases within the stability field of ringwoodite. Increasing pressure has a stronger effect on fO_2 produced by MtW than by NNO leading at 13 GPa to reversed conditions compared to 7 GPa (Fig. 1). At 7 GPa, 1,000°C Fe-ringwoodite broke down at fO_2 of $10^{-7.3}$ bar, while at 13 GPa, 1,000°C Fe, Mg-ringwoodite of composition x_{Fe} = 0.39 (MA-121) is still stable at fO_2 of $10^{-3.9}$ bar but has a higher Fe^{3+} pfu than observed in the more reduced runs, e.g., MA-62 and MA-68[1] (Table 1). Thus, adding Mg increases the stability field of ringwoodite to higher fO_2 compared to the Fe-end-member system (Table 1). The higher Fe^{3+} content in MA-121 compared to MA-68 and MA-62 has been confirmed in a recent study through optical and Mössbauer spectroscopy (Taran et al. 2008). However, the run MA-92 using a Fe-richer composition compared to MA-121 (x_{Fe} = 0.46 versus 0.39) but

[1] In experiment, MA-68 the oxygen fugacity was not controlled but from our experience, we know that our assembly produces relatively reduced conditions between 10^{-11} and 10^{-8}.

also the MtW buffer results in spl and clinopyroxene (cpx). The compositions of coexisting Fe-Mg spl and cpx are given in Table 2. Thus, we observe the same reaction as in the Fe-end-member system: 9 sp = 6 cpx + 5 spl. We notice a high fractionation of Fe into the spl (x^{M}_{Fe} = 0.90) and Mg into the cpx (x^{M}_{Fe} = 0.38) leading to a $K_D = (x_{Mg}^{cpx}\, x_{Fe}^{spl}/x_{Fe}^{cpx}\, x_{Mg}^{spl}) = 14.7$. Run MA-102 performed under QFMt, which under the experimental conditions transformed to SMtFRng, yield st, mt, sp and spl solid solutions. However, as in this experiment the separation of buffer and sample through a Pt disc failed (Table 1) and our run product is more Fe-rich than intended we would exclude this run from the discussion. The presence of the fs in runs MA-47 and MA-75 coexisting with Fe-ringwoodite indicates that the pretreatment of the Pt capsules was not sufficient to prevent total loss of Fe. From the phase relations (about 20 wt% fs) we estimate that 12% of the total iron dissolved into the Pt capsule during the run. Fe loss seems to be less in the shorter run MA-47 than in run MA-75 (Table 1). However, these are only rough estimates as the wt% refined by the Rietveld method must not correspond to the true value (see Table 1). The same holds for the runs where Fe-ringwoodite breaks down to fs and spl as the amount of fs is always higher than expected from the reaction equation. In the more Mg-rich experiments there is with two exceptions no indication of Fe loss: the ringwoodite solid solution of the Fe-richest composition MA-56 has compared to the bulk less Fe than expected which may indicate Fe loss to the wall and MA-62 contains cpx which also may result from Fe loss to the Pt walls. As mentioned before we did not X-ray the entire material but selected only small portions of the run products for the X-ray studies, which can by chance contain different amount of cpx close to the wall. In the microprobe mount no cpx could be detected for MA-62 and MA-56. According to experiments by Johannes and Bode (1978) Fe loss increases with increasing hydrogen fugacity, this and the fact that the other experiments in the olivine system are more Mg-rich may explain that the Fe loss can only be observed in MA-56 and MA-62, the runs with the lowest oxygen fugacity and thus, highest hydrogen fugacity. Due to the iron loss the oxygen fugacity of some of the runs with short run

duration and the Fe-richest compositions (MA-47, MA-56, MA-62), may be not probably controlled but slightly higher then intended: as we observe two competing reactions - Fe loss to Pt and formation of fs versus the buffer reaction. There may not be enough time for the buffer to get the entire capsule in equilibrium. However, from the composition of coexisting fs in run MA-47 ($Fe_{1.98}Si_{2.00}O_3$) there is no indication of oxidation nor from the Fe^{3+}-concentration estimated from microprobe analyses for the coexisting sp of 0.1 pfu (see below). The Mössbauer spectra of run products of MA-62 (IW) and MA-68 (no buffer) yield Fe^{3+}/Fe_{tot} ratios of 0.06 and 0.04, respectively (Taran et al. 2008). O'Neill et al. (1993) report similar ratios of 0.06 and 0.04 for Fe-sp and sp with $x_{Fe} = 0.1$, respectively, in experiments under reducing conditions (IW). They stated that these values represent the minimum possible for these phases under the reduced conditions. This observation is in good agreement with our the Fe^{3+}/Fe ratio calculated for MA-47 of 0.05 and proves the reduced conditions in run MA-47 and the the oxidizing conditions in run MA-121 grown under MtW condition as the ratio in sp from this run is 0.1 (Taran et al. 2008). So, also from these observations there is no indication of oxidation. However, we cannot rule out the possibility that the shortest runs and at the same time the most Fe-rich runs have an oxygen fugacity slightly higher than intended. Nevertheless, we show that sp and sp solid solutions break down to spl and cpx under oxidizing conditions.

The HREM images with lattice fringes and the corresponding diffraction pattern inserted (Fig. 3) taken on (a) (Fe, Mg)-ringwoodite and (b) on spl III show that the crystals are perfect without any defects and mineral or water inclusions. Electron diffraction pattern clearly identify sp and spl. As suggested in the literature we also found that spl III crystallizes in the space group *Imma*.

Figure 4 shows plots of the lattice constants of some run products as a function of composition together with data taken from literature (Ross II et al. 1992; Woodland and

Angel 1998, 2000; Smyth et al. 2003). Figure 4a indicates that with increasing x_{Si} in Fe-ringwoodite the lattice constant *a* decreases. The some holds true for the lattice constants *b* for spinelloid V (Fig. 4c) and spl III (Fig. 4d). For Fe-Mg ringwoodite (Fig. 4b), there is a linear relation between lattice constants and mole fractions of Fe. Ringwoodite with higher Fe^{3+} contents (sample MA-121) of this study at x_{Fe}= 0.39 and one taken from literature at x_{Fe} = 0.10 seem to deviate slightly from this trend to higher values. Infrared spectra in the OH stretching region prove the incorporation of water in sp, spl and cpx (Fig. 5). The absolute water contents are only estimates, as the mineral specific absorption coefficients are not known. However, if such coefficients will exist in future the absolute water contents can be recalculated. As for sp the highest water content (6,500 ppm H_2O by weight) was observed for MA-121 grown under MtW buffer thus with a higher Fe^{3+} content, than samples MA-62 (2,400 ppm), MA-56 (780 ppm) and the Fe-end-member MA-75 (1,000 ppm). If we compare the mean wavenumbers of the OH bands of sp MA-121 with literature data for Mg-rich sp (Smyth et al. 2003), there is a perfect linear correlation. With decreasing x_{Mg} the wavenumber of the OH bands increases. Interestingly, MA-62, MA-56 and MA-75 also show a linear correlation of the mean wavenumber and x_{Mg} but the trend line is quite different to the Mg-rich sp trend line. Obviously, Mg-rich sp does incorporate more water then Fe-rich sp and the water seems to be incorporated in a different way. The OH concentration in spl (1,420 ppm) and coexisting fs (1,410 ppm) (Fig. 5) is in the same range as for the Fe-sp. Interestingly, water is equally distributed between coexisting spl and fs.

Spectra in Fig. 5b collected in the MIR region show the infrared active lattice vibrations of spinel and spinelloid. The Fe-end-member sp spectrum consists of a broad and slightly asymmetric band around 840 cm^{-1}, a weak broad band at 588 and a sharp weak band at 500 cm^{-1}. The strong band around 840 cm^{-1} has been reported for the Mg-sp (830 cm^{-1}), Fe-sp (848 cm^{-1}), Ni-sp (824 cm^{-1}) and Co-sp (825 cm^{-1}) by Akaogi et al. (1984) and Jeanloz (1980) and is assigned to the tetrahedral stretching mode ν_3 (Jeanloz 1980). The sharp band at 500

cm^{-1} has been reported before for the Mg-sp (445cm^{-1}), Fe-sp (503 cm^{-1}), Ni-sp (515 cm^{-1}) and Co-sp (503 cm^{-1}) by Akaogi et al. (1984) and Jeanloz (1980) and is assigned to the tetrahedral bending mode ν_4 (Jeanloz 1980). The latter author reports a shoulder at 568 cm^{-1} for Fe-sp, which is hardly visible in their spectra while we observe a weak but distinct band at 588 cm^{-1}. As the absorbance in our sample was much higher (around 1.5 for the band at 830 cm^{-1} in this study versus 0.8 for the spectrum in Jeanloz 1980) it is possible that the band at 588 cm^{-1} is too weak to be observed in the spectrum of Jeanloz (1980). For Mg-sp Akaogi et al. (1984) report a weak absorption feature at 545 cm^{-1}, which may correlate with our band at 588 cm^{-1}. In the Fe-Mg-sp solid solution MA-68 the main absorbance band is much broader and exhibits a pronounced shoulder at the high-energy side. The band assigned to ν_4 is shifted to 522 cm^{-1} also showing a shoulder at the high-energy side and the weak band is shifted to 600 cm^{-1}. The Raman spectra of ringwoodite of different composition exhibit three distinct bands in all spectra but different in intensity (Fig. 6). In Mg-rich ringwoodite the bands at 843 and 792 cm^{-1} are the strongest while they are very weak but still present in Fe-sp. In Fe-sp the band at 664 cm^{-1} is stronger than the other bands but it is very weak in Mg-rich ringwoodite. The band at 843 cm^{-1} is assigned to pure Si-O bond stretching with A_{1g} symmetry. The bands at 792 and 664 cm^{-1} are due to opposite oscillations of two tetrahedral centers with internal deformations superposed (Yu and Wentcovitch 2006). The two missing Raman bands E_{gg} at 375 cm^{-1} (Mg-sp) and T_{2g} at 309 cm^{-1} (Mg-sp) are very weak and cannot be observed in our spectra.

To our knowledge there is no vibrational study on Fe-spl and we can compare our spectra only with Mg-wadsleyite, the spl III polytype. Infrared spectra of Mg-wadsleyite show strong absorption around 940, 811 and 597 cm^{-1} and weak features at 700 cm^{-1} (Akaogi et al. 1984; Williams et al. 1986; Cynn and Hofmeister 1994; Wu and Wentzcovitch 2007). In the IR spectra of Fe-spl (Fig. 6b) we observe a strong and broad band at 867 cm^{-1} with pronounced shoulders at 959 and 796 cm^{-1}, an intense but broad band at 590 and a weak band at 685 cm^{-1}.

Raman spectra of Mg-wadsleyite show two strong bands at 836 and 850 cm^{-1} (Akaogi et al. 1984) and weak bands at 588, 570 cm^{-1}. In our Raman spectra of Fe-spl (Fig. 7b) we also see very week absorption in the region around 840 cm^{-1} but a stronger contribution at 677 cm^{-1}. The quality of the Raman spectra is low because we used very low laser power and additional filters to avoid melting of the sample under the laser beam. More work is here needed to get a clear picture of the vibrational properties of Fe-spl.

Discussion

Literature data showed that in the system Fe_2SiO_4-Fe_3O_4 three different spl phases labeled spl II, III, and V are stable at pressure of 4-9 GPa and temperature between 900 and 1,200°C. According to Woodland and Angel (2000) the phase relations in this system are complex: at 1,100°C and using an intermediate mixture of fayalite and magnetite spl II was found at low pressure (up to 5 GPa), with increasing P spl III (up to 6 GPa) and, finally spl V (up to 8 GPa) is stable but can also coexist with spl III. In this study, we show that sp and sp solid solutions break down to spl and cpx under oxidizing conditions. This is different to fayalite that breaks down to magnetite plus SiO_2. In agreement with Woodland and Angel (2000) in three of five runs, which produced spinelloid, the spinelloid V modification was built. In run MA-27 and run MA-51, both in the presence of water and at 7 GPa 1,000°C two spl modifications, spl III and V, coexist. Considering the long run duration of MA-27 and the fact that MA-51 used spinel as starting material it seems that the coexistence represents equilibrium. Woodland and Angel (2000) also report on coexisting spl III and V at high pressures.

We observed the sp breakdown reaction also in the Mg_2SiO_4-Fe_2SiO_4 system: with increasing Mg-content the structure of sp seems to accept more Fe^{3+} and is stable at higher fO_2 compared to the Fe-rich sp. In addition with increasing Mg-content increasing amounts of water are incorporated into the sp structure. Whether this increase in water that in case of

ringwoodite is accompanied by an increase in volume (Smyth et al. 2003) favors the increased Fe^{3+} incorporation needs further studies. Sp of composition $x_{Fe} = 0.70$ finally breaks down to spl and cpx at 13 GPa, 1,000°C and MtW conditions. The most of the spl in this experiment crystallize in spl V structure – only 4 wt% are identified as spl III. This is in agreement to Koch et al. (2004) who also observe coexistence of spl III and V at high pressure. According to Koch et al. (2004) the maximum Mg-content of spl III is limited to 15 mol% Mg_2SiO_4 at 7.5 GPa. This is exactly the composition we observed in run MA-92 for spl coexisting with Mg-richer cpx (x_{Fe} =0.38). Different to Koch et al. (2004), who stated that at 1,100°C and above 10 GPa no spl phase was stable, we were able to synthesize spl at 13 GPa and 1,000°C but only from a Fe-rich bulk composition and under MtW buffer conditions. Koch et al. (2004) did not explicitly buffer their experiments and maybe their fO_2-conditions were not high enough to produce spl. Another difference compared to Koch et al. (2004) is that we added water in excess to the experiments and the observed water incorporation into the structures. However, whether this water stabilizes spl to higher pressure needs also further proof. We observed a strong fractionation of Fe into spl and Mg into coexisting cpx. Through this strong fractionation it is possible to stabilize very Fe-rich spl phases with considerable Fe^{3+} concentrations even at an intermediate Fe-Mg bulk composition: if we assume K_D to be independent on composition and a bulk composition of $x_{Fe} = 0.44$ this fractionation would stabilize spl with $x_{Fe} = 0.72$. Thus, spl may be a potential Fe^{3+} bearing phase at P-T conditions of the transition zone provided enough Fe^{3+} is present. However, according to McCammon et al. (2004) oxygen fugacity within the mantle decreases with depth and the bulk concentration of Fe^{3+} is low. They suggest as a more realistic region for the presence of Fe^{3+}- (and OH)-bearing phases subduction zones that are likely oxidized relative to the rest of the mantle. And in addition, in subduction zones Fe-rich bulk compositions are more realistic than in the transition zone. Sp could also break down to magnetite plus SiO_2 - as in the system α-Fe_2SiO_4 - but this must be according to our experiments at higher oxygen fugacities. A breakdown to

magnetite plus SiO_2 would bring free silica to the Earth's mantle, which had important consequences for a number of geophysical and geochemical questions (e.g., Ono et al. 2002). Our study shows that under subduction zone conditions it is more likely that sp breaks down to spl and fs and thus, would be not a source for free silica in the mantle.

The highest water content of the sp phases is found for the most Mg-rich sample of this study (6,500 ppm by wt). This compares well with literature data for the Mg-endmember sp (Ringby2: 7,358 ppm by wt) and an Mg-rich sp (x_{Fe} = 0.11; 10,661 ppm by wt), e.g., Smyth et al. (2004). Water contents in the Fe-rich sp and spl is much less. Thus, with increasing Mg-content there must be a change in the water incorporation mechanism. Such a change is also indicated in the Fig. 7 through the change in the trend lines for the Mg-rich sp and the Fe-rich sp. At a first glance, one would assume that the acceptance of more structural incorporated water is due to the higher acceptance of Fe^{3+} in the structure. However, this is at variance with the results for the Mg-end-member sp, which fits in the trend line for the Fe^{3+} rich samples. A closer look at the water incorporation and water quantification will be the subject of a future study. Preliminary results from SIMS measurements indicate that the quantification using the Libowitzky and Rossman (1997) calibration underestimates the water content.

Reference

Akaogi M, Ross NL, McMillan P et al (1984) The Mg_2SiO_4 polymorphs (olivine, modified spinel and spinel); thermodynamic properties from oxide melt solution calorimetry, phase relations, and models of lattice vibrations. Am Mineral 69:499–512

Akaogi M, Yusa H, Shiraishi K et al (1995) Thermodynamic properties of alpha-quartz, coesite, and stishovite and equilibrium phase relations at high pressures and high temperatures. J of Geophys Res 100:22337–22347

Akimoto S, Ida Y (1966) High-pressure synthesis of Mg_2SiO_4. Earth Plan Sci Lett 1:358–359

Akimoto S, Fujisawa H, Katsura T (1965) The olivine-spinel transition in Fe_2SiO_4 and Ni_2SiO_4. J Geophys Res 70:1969–1977

Chatterjee ND, Krüger R, Haller G et al (1998) The Bayesian approach to an internally consistent thermodynamic database: theory, database, and generation of phase diagrams. Contrib Min Petrol 133:149–168

Chopelas A, Boehler R, Ko T (1994) Thermodynamics and behavior of γ-Mg_2SiO_4 at high pressure: implications for Mg_2SiO_4 phase equilibrium. Phys Chem Min 21:351–359

Cynn H, Hofmeister AM (1994) High-pressure IR spectra of lattice modes and OH vibrations in Fe-bearing wadsleyite. J Geophys Res 99:17717–17727

Fei Y, Bertka CM (1999) Phase transitions in the Earth's mantle and mantle mineralogy. Spec Publ Geochem Soc 6:189–207

Jeanloz R (1980) Infrared spectra of olivine polymorphs; α, β phase and spinel. Phys Chem Min 5:327–341

Johannes W, Bode B (1978) Loss of iron to the Pt-container in melting experiments with basalts and a method to reduce it. Contrib Mineral Petrol 67:221–225

Koch M, Woodland AB, Angel RJ (2004) Stability of spinelloid phases in the system Mg_2SiO_4-Fe_2SiO_4-Fe_3O_4at 1100 °C and up to 10.5 GPa. Phys Earth Planet Inter 143:171–183

Koch-Müller M, Dera P, Fei Y, Reno BL, Sobolev NV, Hauri E and Wysocznaski R (2003) OH^- in synthetic and natural coesite. Am Mineral 88:1436–1445

Koch-Müller M, Abs-Wurmbach I, Rhede D et al (2007) Dehydration experiments on natural omphacites: qualitative and quantitative characterization by various spectroscopic methods. Phys Chem Miner 34:663–678

Larson AC, von Dreele RB (1987) Generalized structure analysis system. Los Alamos National Laboratory Report No. LA-UR-86-748, Los Alamos

Libowitzky E, Rossman GR (1997) An IR absorption calibration for water in minerals. Am Mineral 82:1111–1115

Lloyd EC (1971) Editorial introduction and summary to: accurate characterization of the high pressure environment. US Natl Bur Stand Spec Publ 326:1–3

Ma CB (1974) New orthorhombic phases on the join $NiAl_2O_4$ (spinel analogue)-Ni_2SiO_4 (olivine analogue): stability and implications to mantle mineralogy. Contrib Mineral Petrol 45:257–279

McCammon CA, Frost DJ, Smyth JR, Laustsen HMS, Kawamoto T, Ross NL, van Aken PA (2004) Oxidation state of iron in hydrous mantle phases: implications for subduction and mantle oxygen fugacity. Phys Earth Planet Inter 143-144:157-169

Morishima H, Kato T, Suto M et al (1994) The phase boundary between α- and β-Mg_2SiO_4 determined by in situ X-ray observation. Science 265:1202–1203

Ohtani E (1979) Melting relation of Fe_2SiO_4 up to about 200 kbar. J Phys Earth 27:189–208

O'Neill HStC, McCamon CA, Canil D, Rubie DC, Ross CRII and Seifert F (1993) Mössbauer spectroscopy of mantle transition zone phases and determination of minimum $Fe3^+$ content. Am Mineral 78:456–460

Ono S, Hirose K, Murakami M, Isshiki M (2002) Post-stishovite phase boundary in SiO_2 determined by in situ X-ray observations. Earth Planet Sci Lett 197:187–192

Piermarini GJ, Block S (1975) Ultra high pressure diamond-anvil cell and several semiconductor phase transition pressures in relation to fixed point pressure scale. Rev Sci Instrum 46:973–980

Ringwood AE, Major A (1966) Synthesis of Mg_2SiO_4-Fe_2SiO_4 spinel solid solutions. Earth Planet Sci Lett 1:241–245

Robie RA, Hemingway BS, Fisher JR (1979) Thermodynamic properties of minerals and related substances at 298.15 K and 1 bar (10 Pascal) pressure and higher temperatures. US Geological Survey Bulletin 1452, Washington, DC

Ross CRII, Armbruster T, Canil D (1992) Crystal structure refinement of a spinelloid in the system Fe_3O_4 Fe_2SiO_4. Am Mineral 77:507–511

Schmidt MW, Ulmer P (2004) A rocking multianvil; elimination of chemical segregation in fluid-saturated high-pressure experiments. Geochim Cosmochim Acta 68:1889–1899

Smyth JR, Holl CM, Frost DJ et al (2003) Structural systematics of hydrous ringwoodite and water in Earth's interior. Am Mineral 88:1402–1407

Smyth JR, Holl CM, Frost DJ et al (2004) High pressure crystal chemistry of hydrous ringwoodite and water in the Earth's interior. Phys Earth Planet Inter 143:271–278

Suito K (1972) Phase transformations of pure Mg_2SiO_4 into a spinel structure under high pressures and temperatures. J Phys Earth 20:225–243

Susaki J, Akaogi M, Akimoto S et al (1985) Garnet-perovskite transformation in $CaGeO_3$; in-situ X-ray measurements using synchrotron radiation. Geophys Res Lett 12:729–732

Taran M, Koch-Müller M, Wirth R, Abs-Wurmbach I, Rhede D, Greshake A (2008) Spectroscopic studies of synthetic and natural ringwoodite, γ- $(Mg, Fe)_2SiO_4$. Phys Chem Miner. doi: 10.1007/s00269-008-0271-1

Ulmer O, Luth RW (2006) The graphite-COH fluid equilibrium in P,T, fO_2 space. Contrib Mineral Petrol 106:265-272

van Aken PA, Liebscher B (2002) Quantification of ferrous/ferric ratios in minerals: new evauation schemes of Fe L23 electron energy-loss near-edge spectra. Phys Chem Miner 29:188-200

van Aken PA, Woodland AB (2006) Crystal chemistry of spinel and spinelloid solid solutions in the system Fe_2SiO_4-Fe_3O_4. Geophys Res (abstracts) 8:07770

van Aken PA, Liebscher B, Styrsa VJ (1998) Core-level electron energy-loss spectra of minerals: pre-edge fine structures at the oxygen K-edge. Phys Chem Miner 25:494-498

Walker D (1991) Lubrication, gasketing, and precision in multianvil experiments. Am Mineral 76:1092–1100

Williams Q, Jeanloz R, Akaogi M (1986) Infrared vibrational spectra of beta-phase Mg_2SiO_4 and Co_2SiO_4 to pressures of 27 GPa. Phys Chem Miner 13:141–145

Wirth R (1997) Water in minerals detectable by electron energy-loss spectroscopy EELS. Phys Chem Miner 24:561-568

Woodland AB, Angel RJ (1998) Crystal structure of a new spinelloid with the wadsleyite structure in the system Fe_2SiO_4-Fe_3O_4 and implications for the Earth's mantle. Am Mineral 83:404–408

Woodland AB, Angel RJ (2000) Phase relations in the system fayalite-magnetite at high pressures and temperatures. Contrib Mineral Petrol 139:734–747

Wu Z, Wentzcovitch RM (2007) Vibrational and thermodynamic properties of wadsleyite: a density functional study. J Geophsy Res 112:B12202. doi:10.1029/2007JB005036

Yagi T, Marumo F, Akimoto S (1974) Crystal structures of spinel polymorphs of Fe_2SiO_4 and Ni_2SiO_4. Am Mineral 59:486–490

Yamanaka T (1986) Crystal structures of Ni_2SiO_4 and Fe_2SiO_4 as a function of temperature and heating duration. Phys Chem Miner 13:227–232

Yamanaka T, Okita M (2001) Magnetic properties of the Fe_2SiO_4-Fe_3O_4 spinel solid solutions. Phys Chem Miner 28:102–109

Yamanaka T, Tobe H, Shimazu T et al (1998) Phase relations and physical properties of Fe_2SiO_4 –Fe_3O_4 solid solution under pressures up to 12 GPa. In: Manghnani M,Yogi T (eds) Properties of earth and planetary materials at high pressure and temperature. Geophysical Monograph, Am Geophys Union, Washington, DC, pp 457-459

Yamanaka T, Shimazu H, Ota K (2001) Electric conductivity of Fe_2SiO_4 –Fe_3O_4 spinel solid solutions. Phys Chem Miner 28:110–118

Yu YG, Wentzcovitch RM (2006) Density functional study of vibrational and thermodyamic properties of ringwoodite. J Geophsy Res 111: B12202. doi:10.1029/2006JB004282

Acknowledgements

We would like to thank R. Thomas and S.-M. Thomas for the help with the Raman spectra. H. Steigert and A. Hahn for support with X-ray powder diffraction. G. Berger carefully prepared Microprobe samples. We thank Robert W. Luth and two anonymous reviewers for their suggestions and comments, which improved the quality of the paper.

Figure Captions

Fig. 1 Plots of log fO_2 versus temperature at 1 atm, 7 and 13 GPa for various solid oxygen buffer systems. All systems but one (NNO) were calculated using the database and software by Chatterjee et al. (1998). For NNO we used the thermodynamic data provided by Robie et al. (1979). *FS* ferrosilite, *FRing* Fe-ringwoodite, *I* iron, *Mt* magnetite, *N* nickel, *NO* nickel oxide, *Q* quartz, *S* stishovite, *W* wustite

Fig. 2 a, b Fe-L_3 EEL spectra of spl III and fs, respectively **c, d** O-K edge spectra of spl III and fs, respectively

Fig. 3 Energy filtered, high-resolution transmission electron microscopy images of (Fe, Mg)-ringwoodite MA-62 (**a**) and spinelloid III (**b**) showing the electron diffraction pattern and lattice fringes

Fig. 4 Lattice constants versus composition for

- **(a)** Fe-ringwoodite as function of the mole fraction of Si;
- **(b)** Fe-Mg ringwoodite solid solutions as a function of mole fraction of Fe. *Solid symbols* represent the results of this study. *Open symbols* represent the results taken form literature (adapted from Smyth et al. 2003).
- **(c)** Spinelloid V versus mole fraction of Si. *Open symbols* represent data taken from literature (adapted from Ross II et al. 1992 at $x_{Si} = 0.80$; Woodland and Angel 2000 remaining *open symbols*).
- **(d)** Spinelloid III versus mole fraction of Si. *Open symbols* represent data taken from literature (adapted from Woodland and Angel 1998, 2000)

Fig. 5 a Infrared spectra of ringwoodite (MA-75,-56,-62,-121), spinelloid (MA-27-spl) and ferrosilite (MA-27-fs) in the OH stretching regime. **b** Infrared spectra of ringwoodite (MA-75,-68) and spinelloid III (MA-27) showing lattice modes

Fig. 6 Sequence of Raman spectra of ringwoodite of different compositions and Fe-spinelloid III from different grains. Compared to the ringwoodite spectra, the quality of the spinelloid spectra is much worse because it was much more sensitive to laser damage as ringwoodite. We used very low laser power and additional filters to avoid melting of the sample under the laser beam

Fig. 7 Plot of the mean wavenumber of the OH bands of ringwoodite versus mole fraction of Magnesium indication two different trends: for the most Mg-richest ringwoodite of this study there is a perfect linear correlation between composition and mean wavenumber with literature data ringwoodite with x_{Mg} = 1.0 and 0.88 (adapted from Smyth et al., 2003) but not with the more Fe-rich ringwoodite of this study, indicating a change in the water incorporation mechanism

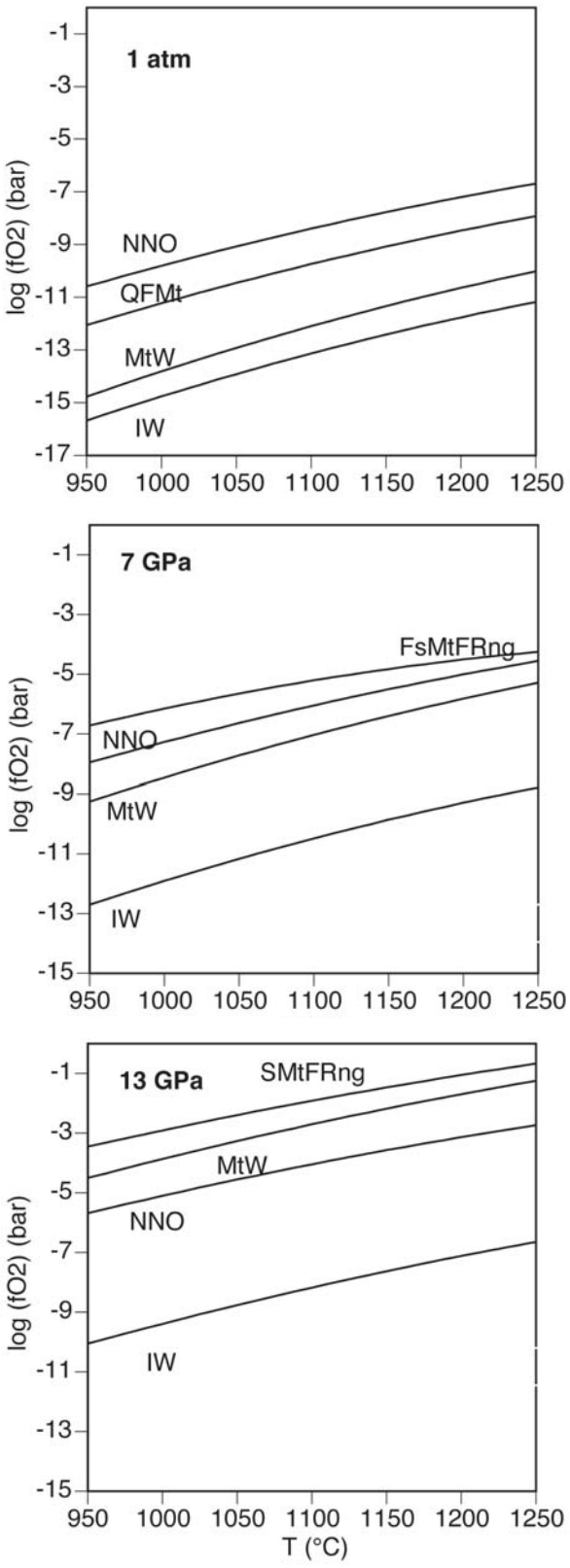

Fig. 1

Fig. 1 Plots of log fO_2 versus temperature at 1 atm, 7 and 13 GPa for various solid oxygen buffer systems. All systems but one (NNO) were calculated using the database and software by Chatterjee et al. (1998). For NNO we used the thermodynamic data provided by Robie et al. (1979). *FS* ferrosilite, *FRing* Fe-ringwoodite, *I* iron, *Mt* magnetite, *N* nickel,

NO nickel oxide, *Q* quartz, *S* stishovite, *W* wustite

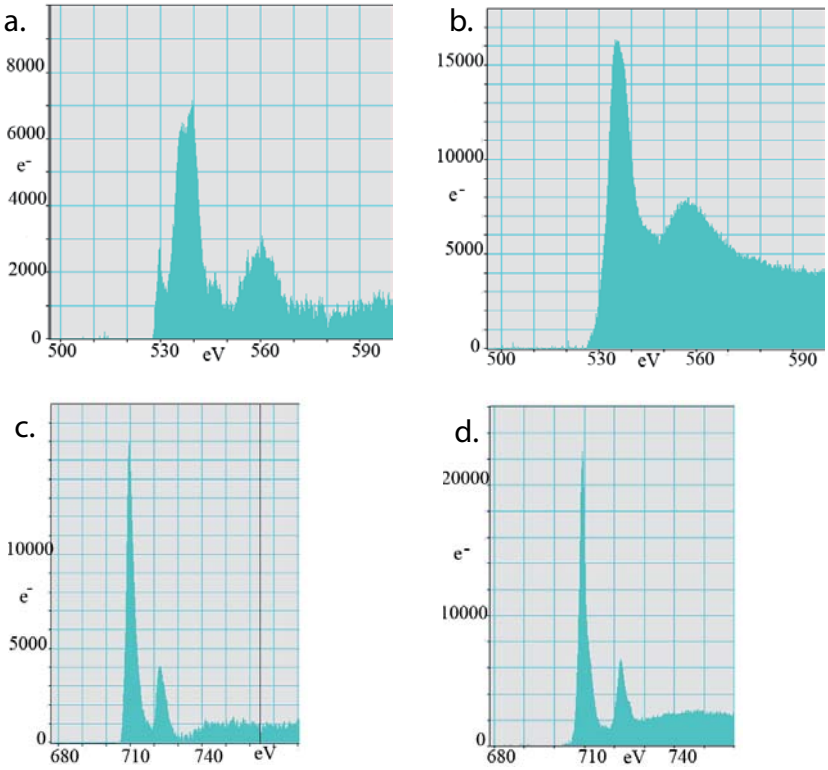

Fig. 2

Fig. 2 a, b Fe-L_3 EEL spectra of spl III and fs, respectively **c, d** O-K edge spectra of spl III and fs, respectively

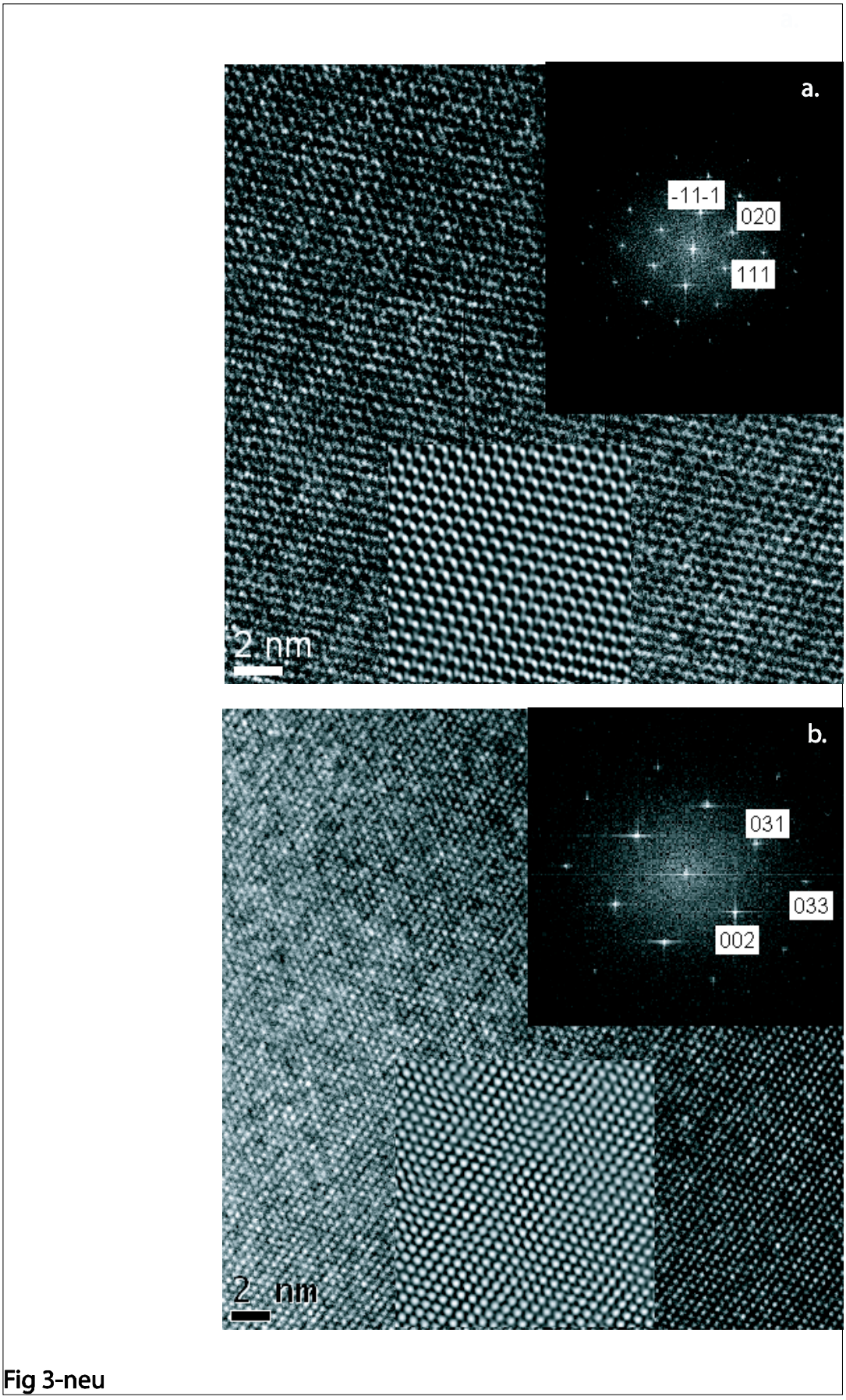

Fig. 3 Energy filtered, high-resolution transmission electron microscopy images of (Fe, Mg)-ringwoodite MA-62 (**a**) and spinelloid III (**b**) showing the electron diffraction pattern and lattice fringes

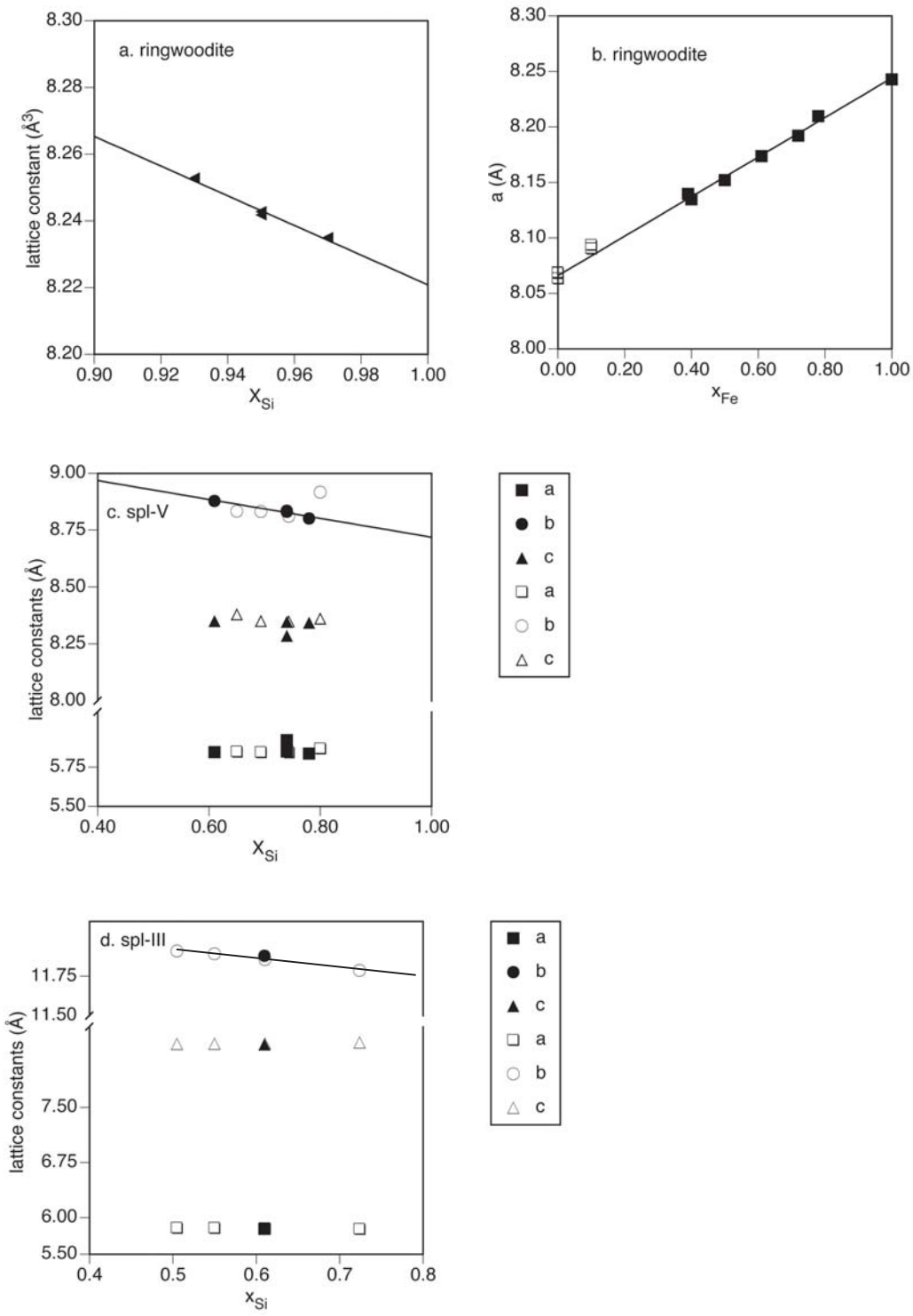

Fig 4

Fig. 4 Lattice constants versus composition for

- **(e)** Fe-ringwoodite as function of the mole fraction of Si;
- **(f)** Fe-Mg ringwoodite solid solutions as a function of mole fraction of Fe. *Solid symbols* represent the results of this study. *Open symbols* represent the results taken form literature (adapted from Smyth et al. 2003).
- **(g)** Spinelloid V versus mole fraction of Si. *Open symbols* represent data taken from literature (adapted from Ross II et al. 1992 at $x_{Si} = 0.80$; Woodland and Angel 2000 remaining *open symbols*).
- **(h)** Spinelloid III versus mole fraction of Si. *Open symbols* represent data taken from literature (adapted from Woodland and Angel 1998, 2000)

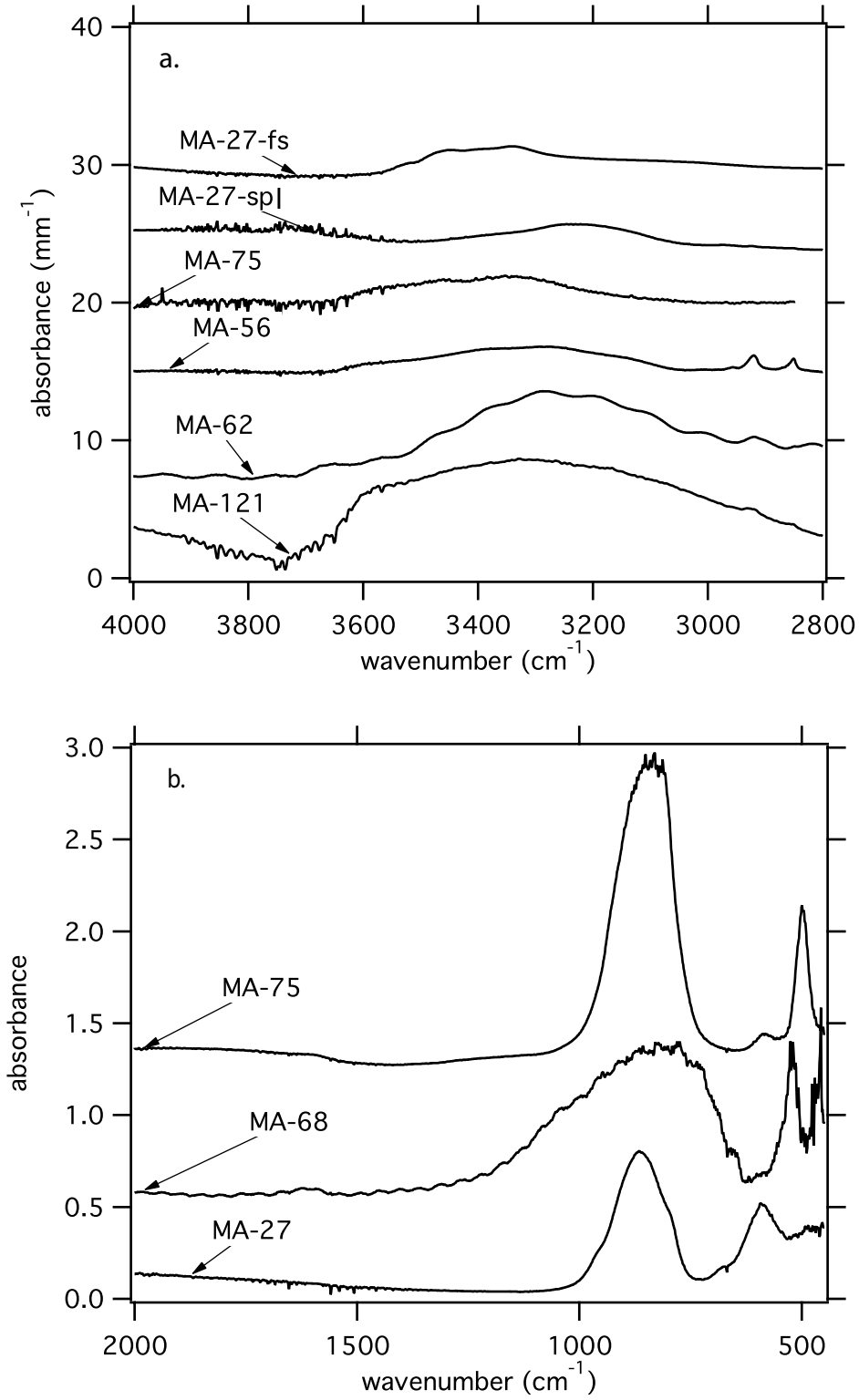

Fig.5

Fig. 5 a Infrared spectra of ringwoodite (MA-75,-56,-62,-121), spinelloid (MA-27-spl) and ferrosilite (MA-27-fs) in the OH stretching regime. **b** Infrared spectra of ringwoodite (MA-75,-68) and spinelloid III (MA-27) showing lattice modes

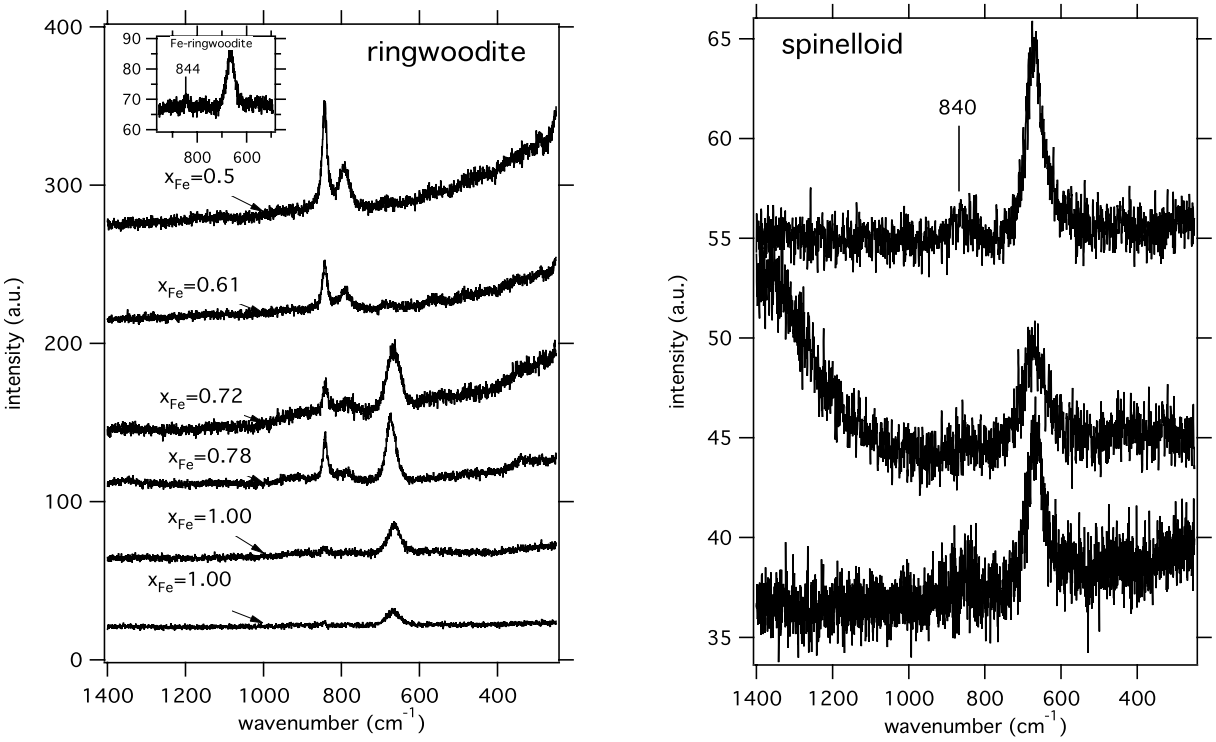

Fig. 6

Fig. 6 Sequence of Raman spectra of ringwoodite of different compositions and Fe-spinelloid III from different grains. Compared to the ringwoodite spectra, the quality of the spinelloid spectra is much worse because it was much more sensitive to laser damage as ringwoodite. We used very low laser power and additional filters to avoid melting of the sample under the laser beam

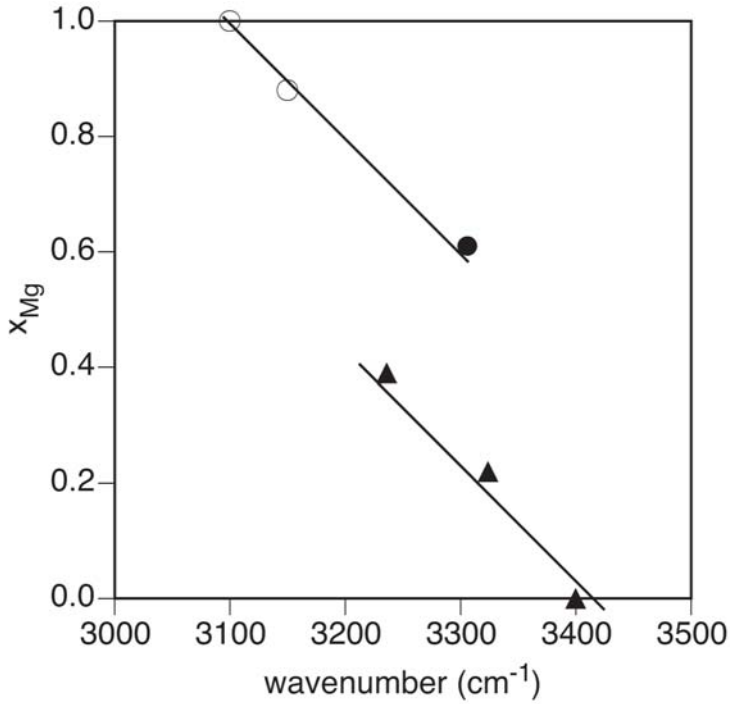

Fig. 7

Fig. 7 Plot of the mean wavenumber of the OH bands of ringwoodite versus mole fraction of Magnesium indication two different trends: for the most Mg-richest ringwoodite of this study there is a perfect linear correlation between composition and mean wavenumber with literature data ringwoodite with x_{Mg} = 1.0 and 0.88 (adapted from Smyth et al., 2003) but not with the more Fe-rich ringwoodite of this study, indicating a change in the water incorporation mechanism

Table 1 Experimental conditions and results of X-ray diffraction

MA	47	22	27[c]	33	36	75	51	56	62[c]	68	92	102[d]	120	121
System	FSH	FSCH	FSH	FS	FSH	FSH	FSH	FMSH	FMSH	FMSH	FMSH	FMSH	FMSH	FMSH
P (GPa)	7.0	6.7	7.0	7.0	7.0	7.0	7.0	13.0	13.0	13.0	13.0	13.0	13.0	13.0
T (°C)	1,000	1,100	1,000	1,000	1,200	1,100	1,000	1,200	1,000	1,000	1,000	1,000	1,000	1,000
Duration (h)	3.5	24	48	24	12	24	24	0.5	4	5.5	3	4	3	3
Starting material	Fayalite, 3 wt% H_2O	Oxid mix, 3 wt% H_2O, graphite	Fayalite, 3 wt% H_2O	Fayalite, dry	Fayalite, 3 wt% H_2O	Fayalite, 3 wt% H_2O	Spinel, 3 wt% H_2O	Oxide mix ($Fay_{80}Fo_{20}$), 5 wt% H_2O	Oxid mix ($Fay_{60}Fo_{40}$), 5 wt% H_2O	Olivine mix ($Fay_{50}Fo_{50}$), 5 wt% H_2O	Olivine mix ($Fay_{70}Fo_{30}$), 5 wt% H_2O	Olivine mix ($Fay_{50}Fo_{50}$), 5 wt% H_2O	Olivine mix ($Fay_{40}Fo_{60}$), 5 wt% H_2O	Olivine mix ($Fay_{40}Fo_{60}$), 5 wt% H_2O
Run Products[a]	sp (84), cfs (16)	spl V (74), cfs (26)	cfs (52), spl III (22), spl V (26)	spl V (49), cfs (51)	sp (68), cfs (15), spl V (16)	sp (74), cfs (26)	sp (88), spl III (8), spl V(4)	sp_{ss} (100), x_{Fe}=0.78	sp_{ss} (88), x_{Fe}=0.61, cpx (11)	sp_{ss} (98), x_{Fe}=0.50	spl V (45), spl III(4), cfs (48), sp (3), x_{Fe}^{spl}=0.85, x_{Fe}^{cpx}=0.38	sp_{ss} (54), x_{Fe}^{sp}=0.72, spl III (20), spl V (4), st (20), Mt (3)	sp_{ss} (100), x_{Fe}=0.40	sp_{ss} (100), x_{Fe}=0.39
fO_2-Buffer (fO_2) bar	IW, $10^{-11.8}$	C-O-H[b], $>10^{-7}$	NNO, $10^{-7.3}$	NNO, $10^{-7.3}$	NNO, $10^{-5.0}$	n.c.	NNO, $10^{-7.3}$	IW, $10^{-7.1}$	IW, $10^{-9.4}$	n.c.	MtW, $10^{-3.9}$	QFMt = SMtFRng, $10^{-2.9}$	NNO, $10^{-5.1}$	MtW, $10^{-3.9}$
χ^2	1.13	1.08	1.05	1.01	0.91	1.05	1.15	0.95	1.04	1.00	1.12	1.17	1.15	1.09
DWd	1.41	1.45	1.48	1.55	1.67	1.42	1.28	1.61	1.48	1.52	1.37	1.30	1.28	1.37
W_{Rp}	0.016	0.014	0.018	0.017	0.019	0.021	0.023	0.022	0.030	0.029	0.020	0.020	0.023	0.028
a (sp)	8.2427 (3)	-	-	-	8.2528 (4)	8.2417 (5)	8.2350 (6)	8.2096 (2)	8.1736 (3)	8.1520 (1)	8.2109 (9)	8.1921 (4)	8.1347 (5)	8.1394 (3)
u (sp)	0.2444 (3)	-	-	-	0.2380 (9)	0.2401 (5)	0.2389 (9)	0.2427 (4)	0.2425 (3)	0.2433 (3)	0.221 (5)	0.2463 (6)	0.2442 (3)	0.2445 (3)
a (spl III)	-	-	5.8440 (9)	-	-	-	5.7595 (26)	-	-	-	5.835 (2)	5.728 (2)	-	-
b (spl III)	-	-	11.8808 (20)	-	-	-	11.6405 (61)	-	-	-	11.707 (3)	11.996 (4)	-	-
c (spl III)	-	-	8.3574 (17)	-	-	-	8.3861 (39)	-	-	-	8.308 (3)	8.333 (3)	-	-
a (spl V)	-	5.8346 (4)	5.8441 (9)	5.9206 (7)	5.8481 (11)	-	-	-	-	-	5.8354 (4)	-	-	-
b (spl V)	-	8.8012 (5)	8.8781 (14)	8.8350 (8)	8.8304 (20)	-	-	-	-	-	8.8721 (8)	-	-	-
c (spl V)	-	8.3429 (5)	8.3502 (12)	8.2857 (6)	8.3473 (17)	-	-	-	-	-	8.3454 (6)	-	-	-

cfs clinoferrosilite, *F* FeO, *Frng* Fe-ringwoodite, *H* H_2O, *I* iron, *M* MgO, *Mt* magnetite, *N* nickel, *n.c.* not controlled but from experiements it is known to be between fO_2 of 10^{-11} and 10^{8} bar, *NO* nickel oxide, *Q* quartz, *QFMt* quartz-fayalite-magnetite, *S* SiO_2, *sp* spinel, *spl* spinelloid, sp_{ss} spinel solid solution, *W* wustite

[a] Numbers in parentheses correspond to the refined wt% in the Rietveld refinement which must not correspond to the true value as only small portions of the run products have been selected for the X-ray diffraction studies

[b] Minimum value calculated according to Ulmer and Luth (2006)

[c] Thermocouple failed and the temperature was estimated ±50°C using power versus temperature calibrations

[d] In this run the separation of the sample from the buffer failed

Table 2 Electron microprobe analyses for ringwoodite, spinelloid and clinopyroxene (1σ)

MA	51[a] sp	47 sp	75[b] sp	56 sp	102 sp	62 sp	68 sp	120 sp	121 sp
FeO	70.92(31)	71.64(70)	70.99(25)	60.54(23)	56.00(38)	49.61(26)	41.60(99)	34.58(37)	34.96(87)
MgO	-	-	0.58(3)	9.40(13)	12.16(25)	18.02 (14)	23.55(98)	28.76(26)	29.11(63)
SiO_2	28.40(22)	27.65(73)	27.86(12)	31.64(14)	32.21(40)	33.47(14)	34.74(32)	35.22(17)	34.86(24)
Σ	99.34	99.29	99.42	101.58	100.38	101.10	99.89	98.55	98.93
	Calculated Fe_2O_3 to adjust the stoichiometry								
FeO	69.02	68.12	67.52	-	-	-	-	33.52	32.70
MgO	-	-	0.58	-	-	-	-	28.76	29.11
Fe_2O_3	2.12	3.91	3.86	-	-	-	-	1.2	2.5
SiO_2	28.40	27.65	28.27	-	-	-	-	35.22	34.86
Σ	99.55	99.69	99.81	-	-	-	-	98.67	99.18
	Cations per formula unit								
Fe^{2+}	1.98(1)	1.95(2)	1.92(1)	1.58(1)	1.4 (1)	1.23(1)	0.99(4)	0.79 1)	0.76(2)
Mg	-	-	0.03(1)	0.44(<1)	0.56(1)	0.79(<1)	1.01(4)	1.20(1)	1.21(2)
Fe^{3+}	0.05(2)	0.10(4)	0.10(<1)	-	-	-	-	0.03(<1)	0.05(<1)
Si	0.97(1)	0.95(2)	0.95(1)	0.99(1)	1.00(1)	0.99(1)	1.00(11)	0.99(1)	0.97(1)
Σ	3.00	3.00	3.00	3.00	3.00	3.01	3.00	3.00	3.00
x_{Fe}	1.00	1.00	0.99	0.78	0.72	0.61	0.50	0.40	0.39
MA	22 spl	27 spl	33 spl	33 cpx	36 spl	36 sp	92 spl	92 cpx	92 sp
FeO	76.34(99)	80.1(99)	77.43(75)	54.56(38)	77.06(30)	72.48(86)	74.44(99)	24.77(86)	40.10(62)
MgO	-	-	-	-	-	-	6.00(32)	22.43(57)	25.76(74)
SiO_2	22.52(92)	17.33(97)	21.26(61)	45.20(20)	21.09(8)	27.35(78)	18.16(95)	53.55(39)	34.19(28)
Σ	98.12	97.77	98.68	100.00	98.21	99.84	98.60	100.75	100.07
	Calculated Fe_2O_3 to adjust the stoichiometry								
FeO	61.67	54.66	59.72	-	59.5	67.91	46.80	24.35	37.90
MgO	-	-	-	-	-	-	6.00	22.43	25.76
Fe_2O_3	16.30	28.34	19.68	-	19.52	5.08	30.72	0.47	2.45
SiO2	22.52	17.33	21.26	-	21.09	21.09	18.16	53.55	34.19
Σ	100.49	99.69	100.69	-	100.17	100.17	101.67	100.79	100.29
	Cations per formula unit								
Fe^{2+}	1.79(3)	1.62(3)	1.74(3)	1.01(1)	1.75(1)	1.94(3)	1.32(2)	0.38(3)	0.90(2)
Mg	-	-	-	-	-	-	0.3 (2)	0.62(3)	1.09(3)
Fe^{3+}	0.43(6)	0.76(7)	0.52(4)	-	0.52(1)	0.1 (5)	0.78(6)	0.01(<1)	0.05(<1)
Si	0.78(3)	0.61(3)	0.74(2)	1.00(1)	0.74(1)	0.93(3)	0.61(3)	1.00(<1)	0.97(<1)
Σ	3.00	3.00	3.00	2.00	3.00	3.00	3.00	2.00	3.01
x_{Fe}	1.00	1.00	1.00	1.00	1.00	1.00	0.85	0.38	0.46

[a] A few grains of the total charge were contaminated with Ni (about 1 wt% NiO). Most probably they were in contact with the buffer material. The most of the charge was, however, Ni free

[b] The starting material was aimed to contain no Mg, but obviously some contamination with Mg must have occured (parts from the assembly) before the run. We can excluded contamination of the charge during the run as the presence of water after opening the capsule indicates that it was closed during the run